High-performance hydrogenated amorphous silicon deposited by ion-beam sputtering for gravitational-wave detectors

Shenghuan Fang, Zhenyin Lu, Xiaochuan Ji, Hongfei Jiao,
Xinbin Cheng, Zhanshan Wang, and Jinlong Zhang*

Institute of Precision Optical Engineering, School of Physics Science and Engineering, Tongji University, Shanghai, 200092, China
and MOE Key Laboratory of Advanced Micro-Structured Materials, Shanghai 200092, China

(Received 15 July 2023; accepted 15 August 2023; published 1 September 2023)

Amorphous silicon (a-Si) is a promising material with a high refractive index that shows great potential in the development of low-thermal-noise, highly reflective coatings for gravitational-wave detectors due to its low mechanical loss. However, its high optical absorption has hindered its practical use. The primary objective of this paper is to investigate the effects of hydrogen incorporation into a-Si on its optical properties and mechanical loss with ion-beam sputtering (IBS) technology, which is widely used to produce coatings with low absorption and scattering loss. It is demonstrated that hydrogenation can effectively reduce the optical absorption of a-Si, with the concentration of hydrogen proving to be a crucial factor. Optimal annealing temperature can further enhance the coating quality, in which silicon atom rearrangement also contributes to the improvement. Overall, using the process combination can reduce the extinction coefficient of a-Si coatings by 16-fold at 1064 nm and 85-fold at 1550 nm, while simultaneously reducing mechanical loss by a factor of 12. The degree of mechanical loss reduction is closely related to the order present in the atomic structure of the silicon network. To our knowledge, this study represents the first comprehensive analysis of coating mechanical loss in hydrogenated a-Si deposited via IBS.

DOI: 10.1103/PhysRevD.108.062002

I. INTRODUCTION

Ultrastable optical cavities are crucial for performing high-precision measurements using laser interferometers, including gravitational-wave (GW) detectors [1], femtosecond optical atomic clocks [2], laser gyroscopes [3], and cavity ring-down spectroscopies [4]. Among these, GW detectors have garnered extensive attention as one of the most cutting-edge tools in astrophysics ever since the first detection of a GW signal in 2015 [5]. However, the Brownian motion of atoms in the coatings of ultrastable optical cavities results in thermally driven fluctuations in the separation between the optical resonator mirrors, which limits the achievable sensitivity of these applications. This phenomenon is known as coating thermal noise (CTN) [6,7]. According to the fluctuation-dissipation theorem [8], the power spectral density of CTN is proportional to the mechanical loss of the coating materials, the thickness of coating, and the temperature of the mirror,

$$S_{\text{CTN}} \propto \frac{k_B T d}{2\pi f \omega^2} \varphi_{\text{coating}}(f), \tag{1}$$

where k_B is the Boltzmann constant, T is the temperature of the mirror, d is the thickness of coating, $\varphi_{\text{coating}}(f)$ is the mechanical loss of the coating materials, f is the frequency, and ω is the laser beam radius.

Highly reflective (HR) coatings are usually thickness-optimized stacks composed of alternating layers of coating materials with high and low refractive indices, forming the core of optical cavities. And the high-refractive-index materials used in HR coatings generally have higher mechanical loss angles than the low-refractive-index materials, which dominate the overall mechanical loss of the HR coatings [9–11]. To reduce the mechanical loss of HR coatings designed for the operating wavelength of 1064 nm at room temperature, titania-doped tantala ($TiO_2:Ta_2O_5$) has been chosen as the high-index material in Advanced LIGO [12] and Advanced Virgo [13]. Nevertheless, the $TiO_2:Ta_2O_5$ material used in present GW detectors displays a noticeable peak in mechanical loss at low temperatures [14,15], limiting its application in future GW detectors in low-temperature environments, such as KAGRA [16,17] and the European Einstein Telescope [18–21]. To address this challenge, several ongoing research works aim to identify a substitute for the $TiO_2:Ta_2O_5$ high-index material, characterized by higher refractive index, lower mechanical loss, and comparable low absorption properties.

Amorphous silicon (a-Si) demonstrates high potential as a high-index material due to its higher refractive index and

*jinlong@tongji.edu.cn

 © 2023 American Physical Society

lower mechanical loss when compared to $TiO_2:Ta_2O_5$. This makes it easier to reduce the CTN of HR coatings by decreasing both the mechanical loss and thickness of the coatings. Additionally, a-Si features low mechanical loss at room temperature and even lower loss at colder temperatures [22,23], which makes it particularly well-suited for low-temperature applications in future GW detectors. Despite its advantages, a-Si has a significant drawback as its optical absorption is notably higher than that of $TiO_2:Ta_2O_5$ at the wavelength of 1064 nm [24,25], which the present GW detectors are illuminated at. Although its absorption can be smaller at 1550 nm, which is a possible and appealing working wavelength for future GW detectors, the present absorption level still exceeds requirements [25–28]. To prevent the heating and thermal deformation of mirrors in ultrastable optical cavities, the optical absorption level of HR coatings must be less than several ppm. Several strategies exist to enhance the absorption performance of a-Si, including different coating preparation techniques [26–28], postdeposition heat treatment [25–27], or introducing hydrogen into a-Si [29–32]. Additionally, multimaterial coating designs can reduce the impact of unsatisfactory absorption by using other low-absorption materials to replace the upper layers of HR coatings [33–35]. By doing so, the absorption requirements of silicon-based mirror coatings can be prominently relaxed, making the use of a-Si in future GW detectors more feasible.

In applications with strict requirements for coating performances, researchers typically utilize ion-beam-sputtering (IBS) technology to achieve excellent optical properties, including low absorption and low scattering loss, similar to the process used by the Laboratoire des Matériaux Avancés (LMA) in producing HR coatings for Advanced LIGO and Advanced Virgo [36,37]. The IBS-deposited coatings have almost no inherent film roughness, leading to reduced scattering loss and allowing for a lower noise level and improved resolution in GW detectors. Developing an IBS process that effectively reduces a-Si absorption is a worthy pursuit as it can build upon the current successes of IBS technology, seamlessly integrate with low refractive index materials deposited through established IBS techniques, and eliminate engineering challenges commonly associated with other methods. The hydrogen incorporation into a-Si during IBS deposition has been attempted to alter optical properties of a-Si [30–32]. And previous researches have indicated that hydrogen can significantly reduce the mechanical loss of a-Si, even by several orders of magnitude at low temperatures [38–40]. Nonetheless, to the best of our knowledge, none of these investigations have explored the effects of hydrogen on coating mechanical loss of a-Si deposited by IBS. It can be expected that depositing a-Si with hydrogen (i.e., hydrogenated amorphous silicon) by IBS will improve both its optical absorption and mechanical loss, and the processes involved in introducing hydrogen are worth exploring and studying.

In this paper, we propose IBS deposition processes to prepare high-quality a-Si coatings achieved by incorporating hydrogen, resulting in reduced absorption and mechanical loss, and maintaining low surface roughness. By feeding hydrogen gas to the surface of a silicon target or an ion source during deposition, we can decide whether to introduce hydrogen as molecules or high-energy ions. We have conducted a systematic examination and comparison of the effects of these two ways to incorporate hydrogen into a-Si on its optical properties, surface morphologies, and mechanical loss, as well as the influences of annealing on these characteristics of a-Si and hydrogenated a-Si coatings. The optical constants at the wavelength of 1064 nm and mechanical loss at room temperature are the main concerns in our work, which is the operating condition of the present GW detectors. The extinction coefficient at 1550 nm is also presented, which is an important wavelength of more interest in the future GW detectors such as Einstein Telescope [20,21] and Cosmic Explorer [41]. The short-range order (SRO) and medium-range order (MRO) of the silicon atomic structures of a-Si and hydrogenated a-Si coatings have been characterized to gain a better understanding of the mechanisms of coating mechanical loss at the atomic scale. To our best knowledge, we show the mechanical loss measurements of a series of hydrogenated a-Si coatings deposited by IBS for the first time.

II. SAMPLE PREPARATION

All a-Si and hydrogenated a-Si coatings were produced in our institute. Single thin layers of a-Si and hydrogenated a-Si coatings were deposited on germanium substrates (ϕ 1″, 1 mm thick) to measure their Fourier transform infrared (FTIR) transmission spectroscopy, on fused-silica substrates (ϕ 1″, 5 mm thick) to measure their optical properties, surface morphologies, and atomic structures, and on fused-silica substrates (ϕ 3″, 1 mm thick) for mechanical loss measurements. All coatings were deposited by a commercially available IBS coater (SPECTOR-HT, Veeco) with a 16 cm Kaufman-type ion source and a 12 cm one. An argon ion beam with a diameter of 16 cm was used to sputter the material from the crystalline silicon target. To prepare the hydrogenated a-Si coatings, two alternative conditions to incorporate hydrogen were used: (a) when 12 cm ion source was inactive, variable flow rates of hydrogen gas were fed to the surface of silicon target; (b) 12 cm ion source was active with a gas mixture of hydrogen and argon fed. The feeding position of hydrogen gas determined whether hydrogen was introduced into silicon network as molecules or as ions. For the 16 cm ion source, the beam voltage, beam current, and accelerator voltage were 600 V, 300 mA, and 400 V, respectively. And for 12 cm ion source, those were 300 V, 150 mA, and 400 V,

TABLE I. List of the relevant deposition parameters and measurement results of as-deposited a-Si and hydrogenated a-Si coatings.

				$k \times 10^{-3}$		n		
Name	Destination of H_2	Flow rate of H_2 (sccm)	Thickness (nm)	1064 nm	1550 nm	1064 nm	1550 nm	$\varphi_m \times 10^{-4}$[a]
A00	/	0	797	66.0	22.4	3.84	3.68	2.43
T10	Target	10	746	30.7	10.5	3.58	3.43	1.19
T20	Target	20	747	16.5	3.91	3.44	3.32	1.69
T50	Target	50	708	6.51	1.06	3.40	3.30	1.51
T75	Target	75	718	5.99	1.90	3.03	2.95	1.54
I10	Ion source	10	795	47.1	10.6	3.83	3.67	1.69
I20	Ion source	20	741	5.76	0.989	2.93	2.86	1.29
I50	Ion source	50	775	9.64	2.44	3.20	3.11	1.72

[a]The measurement results of mechanical loss were averaged on different resonant modes for better comparison.

respectively. In the case of 12 cm ion source inactive, 0 sccm, 10 sccm, 20 sccm, 50 sccm, and 75 sccm of hydrogen flow rates were chosen to modify the hydrogen content in hydrogenated a-Si coatings. For the mixed gas to the active 12 cm ion source, the flow rates of hydrogen ranged from 10 sccm to 50 sccm, with keeping 8 sccm of argon gas. The mixing with 8 sccm of argon gas was used to make the 12 cm ion source work normally and stably. The base pressure was 2×10^{-6} Torr, while the working pressure was kept in the level of 10^{-4} Torr during deposition. The details and preparation parameters of as-deposited a-Si and hydrogenated a-Si coatings are summarized in Table I. In this paper, we name the kind of samples with hydrogen introduced to silicon target as series T and the others with hydrogen fed into 12 cm ion source as series I, which means hydrogen is introduced as molecules in series T and as high-energy ions in series I. The numbers in the names represent the corresponding flow rate of hydrogen during the deposition process. In order to obtain a sufficient number of samples for different treatments or tests on the same type of coatings, a batch of samples, with a certain quantity, were deposited in the same chamber of an IBS coater at the same time, which are called “companion samples”. Different types of coatings have different batches of companion samples. The coatings on the same batch of companion samples can be considered identical.

To investigate the effects of postdeposition heat treatment temperature on optical and mechanical properties of coatings, three annealing temperatures were chosen. Some companion samples were annealed, respectively, at 300 °C, 400 °C, and 500 °C in air for one hour, while other samples with no heat treatment are referred to as the “as-deposited” samples in this paper. After heating, samples underwent naturally cooling in the environment where they had been annealed. No matter whether samples were annealed or not, all samples were not sealed or otherwise specially treated for storage. Rather, a layer of native oxide was allowed to form, which was estimated to be less than 2–3 nm [42] and effectively prevented our samples from further absorbing oxygen and water.

III. EXPERIMENTAL METHODS

Respective companion samples of all types of a-Si and hydrogenated a-Si coatings were examined by the following measurement techniques.

The FTIR transmission spectra were measured in the wavenumber range of 500–2300 cm^{-1} by a FTIR spectrometer (INVENIO S, Bruker) with a resolution of 2 cm^{-1} to estimate hydrogen concentration contained in hydrogenated a-Si coatings. The reflectance and transmittance spectra of each sample were measured from 400 to 2600 nm by a spectrophotometer (Cary 5000, Varian). Based on fitting the experimental data of spectra, the refractive index, extinction coefficient, and thickness of the samples were derived by Optichar, an optical characterization module from Optilayer (OptiLayer GmbH) [43]. The precision of deduced refractive index and extinction coefficient was estimated at ±0.01 and ±0.0001, respectively [44]. The surface morphologies were obtained by atomic force microscopy (Dimension Icon, Bruker) and were evaluated by surface root mean square (RMS) roughness. The size of scanning area was 20 μm × 20 μm, and consisted of 512 × 512 sampling point matrix. We also observed the surface of our samples through the optical microscope (DM 4000 M, Leica) to determine whether there were obvious defects, such as cracks. To probe the SRO and MRO of atomic structures, cross section samples of a-Si and hydrogenated a-Si coatings were prepared by a dual beam system focused-ion-beam scanning electron microscope (Helios 5 DualBeam, FEI) and were then characterized by a transmission electron microscope (Talos F200X, FEI) to collect selected-area electron diffraction (SAED) data at an accelerating voltage of 200 kV. Reduced density functions (RDF) were directly computed from electron diffraction intensities to describe atomic structures of amorphous coatings.

Mechanical loss can be analyzed from the free exponential decay of vibration amplitude of samples’ resonant modes, by measuring the corresponding resonant frequency and characteristic decay time. For the resonant frequency f

and decay time τ, the measured mechanical loss is $\varphi = (\pi f \tau)^{-1}$. A gentle nodal suspension (GeNS) design in a vacuum chamber was used to achieve a clamp-free condition and minimize the effect of systematic damping from suspension and residual gas pressure [45]. With GeNS, mechanical loss measurements of disk-shaped samples were performed. We excited four resonant modes of each sample at room temperature by an electrostatic actuator, detected the vibration motions with an optical lever system, and then obtained the mechanical loss angles at resonant frequencies. These resonant modes we selected were of the same family, namely pure butterfly modes, in order to better compare the changes of coating mechanical loss with different preparation processes and treatments. Coating mechanical loss can be calculated from the difference between the measured mechanical loss angles of disc samples before and after coating [46], according to the relation written as

$$\varphi_{\text{coating}} = \frac{\varphi_{\text{coated}} + (D-1)\varphi_{\text{substrate}}}{D}, \tag{2}$$

where φ_{coating}, φ_{coated}, and $\varphi_{\text{substrate}}$ are, respectively, the mechanical loss angles of the coating, the coated sample, and the bare substrate. Each substrate's loss angle was measured before coating and was usually assumed to maintained unchanged during the deposition process. D is the frequency-dependent dilution factor, defined as [47]

$$D = \frac{E_{\text{coating}}}{E_{\text{coating}} + E_{\text{substrate}}}, \tag{3}$$

where E_{coating} is the elastic energy stored in the coating while $E_{\text{substrate}}$ is the one stored in the substrate. This factor D can be calculated by finite element analysis software. In our work, we used COMSOL Multiphysics finite element analysis program [48] to obtain the elastic energies stored in the coating and substrate, respectively.

IV. RESULTS AND ANALYSIS

A. Hydrogen concentration

The FTIR transmission spectra of as-deposited samples are shown in Fig. 1. We also plot the data of Ge substrate we used for comparison. There are three typical absorption regions related to hydrogen in hydrogenated a-Si coatings. The absorption region centered around 640 cm^{-1} is related to wagging mode of monohydrogen complexes (Si─H) [49,50], while the region around 800–900 cm^{-1} is related to doublet bending and scissor modes of polyhydride complexes $(\mathrm{Si-H_2}$ and $(\mathrm{Si-H_2})_n)$ [51,52]. And the absorption band approximately at 1900–2200 cm^{-1} is associated with stretching modes corresponding to Si─H and $(\mathrm{Si-H_2})_n$ [53,54]. The absorption peak around

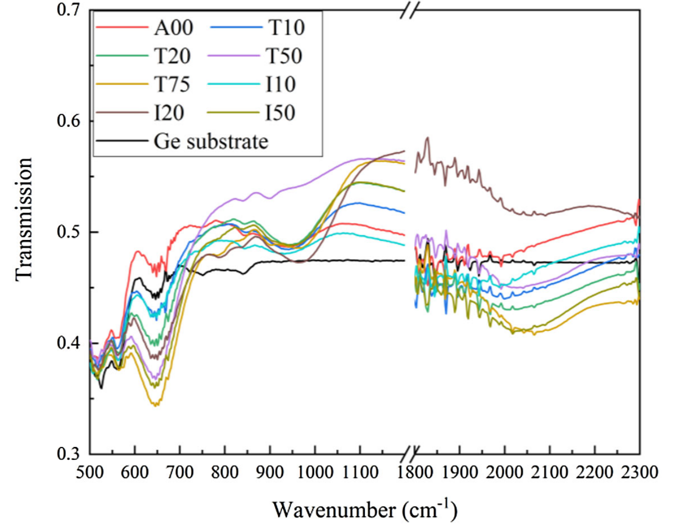

FIG. 1. FTIR transmission spectra for various H_2 flow rates and different ways to incorporate hydrogen.

950 cm^{-1} indicates some degree of oxygen contamination was contained in the samples [32,55].

To estimate the hydrogen concentration, the absorption coefficient is calculated from FTIR transmission spectra, following Maley's method [56]. The FTIR absorption spectra are shown in Fig. 2. The total hydrogen concentration C_H bonded to silicon is proportional to the absorption band of wagging mode around 640 cm^{-1}, which is independent of the bonding configurations. C_H can be calculated by [57]

$$C_H = 100\% \times \frac{A_{640} \times \int \alpha(\omega)\omega^{-1} d\omega}{A_{640} \times \int \alpha(\omega)\omega^{-1} d\omega + N_{\text{Si}}}, \tag{4}$$

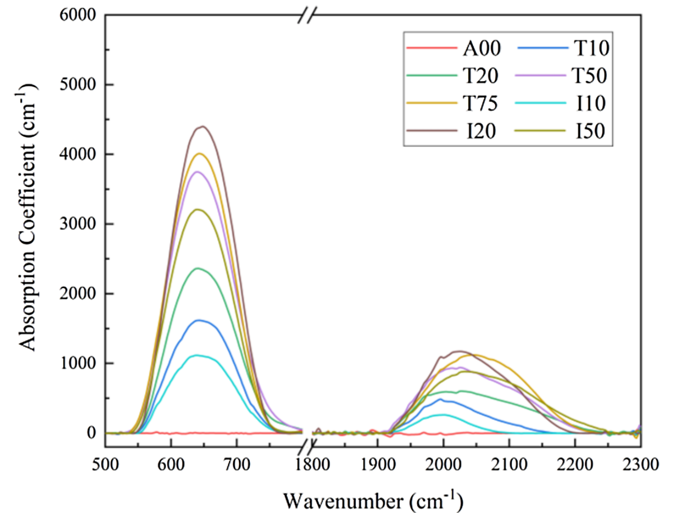

FIG. 2. FTIR absorption spectra for various H_2 flow rates and different ways to incorporate hydrogen.

TABLE II. The total hydrogen concentrations of as-deposited and annealed samples.

	Total hydrogen concentration (at.%)			
Name	As—deposited	Annealed at 300 °C	Annealed at 400 °C	Annealed at 500 °C
A00	0.0	0.0	0.0	0.0
T10	10.84	11.22	6.60	3.64
T20	15.47	15.85	9.38	6.43
T50	22.23	18.53	11.96	9.32
T75	22.88	17.00	11.84	9.15
I10	7.76	8.12	8.33	4.43
I20	24.17	19.73	14.05	8.63
I50	19.39	19.30	14.93	9.16

where $\alpha(\omega)$ is the absorption coefficient, ω is the wavenumber in cm^{-1}, $A_{640} = 2.1 \times 10^{19}\ \mathrm{cm}^{-2}$ is proportionality constant, and $N = 5.0 \times 10^{22}\ \mathrm{cm}^{-3}$ is the atom density of silicon film. The calculation results of as-deposited samples are shown in Table II. For feeding hydrogen to silicon target, it is obvious that C_H increases with the increasing hydrogen flow rates. It can be understood that the more hydrogen molecules near the target or in the chamber, the higher the probability that hydrogen can be bonded to silicon atoms. This increases the hydrogen contents contained in coatings. For feeding hydrogen into 12 cm ion source, C_H increases first and then decreases with more hydrogen fed. It might be explained by the bond breaking action of high-energy hydrogen ions, including the breaking of Si—Si bond and Si—H bond. Since the average bond energy of Si—Si is less than that of Si—H, the probability of high-energy hydrogen ions breaking Si—Si bond is greater than that of breaking Si—H bond. At first, the increase of hydrogen flow rates leads to the increase of Si—H bonding probability. Whether Si—H bonding is caused by direct bonding of Si atoms and hydrogen ions or by high-energy hydrogen ions breaking Si—Si bonds, it leads to the increase of C_H in the coatings. Then, with the further increase of the flow rates, more and more high-energy hydrogen ions begin to break partial Si—H bonds and extract hydrogen from the forming surface of hydrogenated a-Si coating to produce hydrogen molecules during deposition process, so C_H decreases from sample I20 to I50. The role of high-energy hydrogen ions in breaking Si—H bond can be outstanding when we compare the two ways of incorporating hydrogen. The samples T10 and T50 contain more hydrogen than those with the same hydrogen flow rates to ion source. For the sample I20, the maximum C_H may result from the additional increase of hydrogen molecules near the forming surface of hydrogenated a-Si due to breaking function.

After annealing hydrogenated a-Si coatings, all FTIR transmission spectra have similar changes. Taking sample T50 as an example, we show the representative influences of postdeposition heat treatment temperature in Fig. 3.

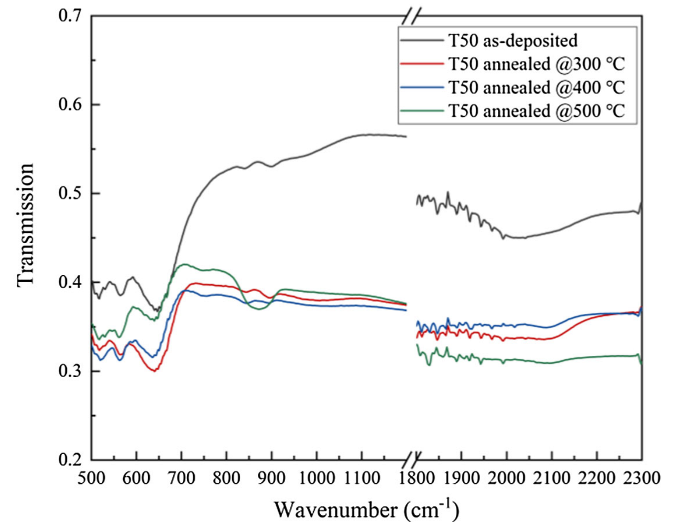

FIG. 3. Representative changes of FTIR transmission spectra after annealing.

With the increase of annealing temperature, the infrared absorption around 640 cm^{-1} changes gradually, and after annealing at 500 °C, a new absorption peak appears near 875 cm^{-1}, which corresponds to Si—OH bond [58]. The results of C_H after annealing are also listed in Table II. It can be found that C_H decreases with the increasing temperature for samples T50, T75, I20, and I50 with high C_H, while C_H first increases slightly and then decreases for low-C_H samples T10, T20, and I10. After annealing at 500 °C, most of hydrogen elements escape out of hydrogenated a-Si coatings. Since hydrogen diffusion is a thermally activated process, at an annealing temperature of 500 °C, hydrogen obtains sufficient thermal activation energy, resulting in a high diffusion coefficient and a great evolution from coatings. We observed that for samples with high C_H, the trends of C_H variation were similar to those shown in Ref. [59], despite the fact that they were prepared by different technologies for hydrogenated a-Si coatings. It is known that annealing can also result in the diffusion, relocation, and rebinding of hydrogen [59–63], accompanied by hydrogen evolution. Due to the delicate process, there is no clear rule for determining the reduction proportion of C_H or residual C_H. However, it can be observed that the amount of C_H reduction caused by postdeposition heat treatment appears to be greater if the C_H contained in corresponding as-deposited samples is higher. The greater reduction in samples with higher C_H may be related to nanovoids [61,64], low mass density [61], and hydrogen chemical potential [63]. These factors can result in a higher hydrogen diffusion coefficient and greater hydrogen evolution. For samples with low C_H, a little increase in C_H after annealing at 300 °C or 400 °C may be attributed to hydrogen molecules in the nanovoids diffusing into the silicon structure and forming Si—H bonds during heat

treatments, while the rates of hydrogen evolution are not high at these temperatures.

B. Optical properties

1. Refractive index

Figure 4 illustrates the refractive index n of our as-deposited samples in series T and I. The results indicate that all processes of hydrogen incorporation reduce n of a-Si in the as-deposited samples. In series T, we observe a gradual decrease in n with increasing hydrogen flow rates. In series I; however, we observe an initial decrease in n followed by a slight increase with higher H_2 flow rates. If we focus solely on the relationship between the H_2 flow rates and n in series T or I, we can see that this in fact corresponds to the relationship between C_H and n. In Fig. 4, we also include the C_H results of the as-deposited samples. It is shown that there is a decrease in n as the C_H increases in the respective series of series T or series I. The changes in the flow rates correspond to variations in the C_H of the coatings. Furthermore, n may be related to the mass density of the material [65]. It suggests that a higher C_H leads to a less dense coating. This is likely due to an increased propensity for hydrogen atoms to bond with silicon atoms, as compared to silicon atoms bonding with other silicon atoms. This phenomenon results in the "hydrogen substitution" for silicon atoms, which can lead to changes in the mass density of coatings. The changes in mass density with C_H can be described by a combination of the monovacancy model and divacancy model [64]. Furthermore, as shown in Ref. [64], hydrogenated a-Si coatings may contain nanovoids and the presence of nanovoids may increase with higher C_H. Additionally, excessive hydrogen exposure on the forming coating surface may result in the breakage of weak Si─Si bonds, a phenomenon known as "hydrogen etching" [66,67]. This could also lead to an increase in the fraction of nanovoids in coatings with higher C_H, further contributing to the reduction in refractive index.

Upon comparison of the hydrogen content and refractive index data for all samples in series T and I, it becomes apparent that there is an inverse relationship between n and C_H for most samples. However, this relationship does not hold true for samples T50 and I50. This implies that the hydrogen ions in series I have additional functions. In general, the ions from the 12 cm ion source can further provide kinetic energy to produce denser films. However, due to that the average bond energy of Si─Si is less than that of Si─H and hydrogen makes the energy barrier lower [68], high-energy hydrogen bombardment may break the weak Si─Si bonds in addition to transferring kinetic energy. This is similar to "hydrogen etching", but more likely to result in more nanovoids formation and lower mass density. It may explain the abnormal situation that the two samples T50 and I50 deviate from the relationship between C_H and n. Comparing the two ways of incorporating hydrogen into a-Si coatings, the function of energetic hydrogen ions to reduce mass density is more obvious than the function to produce denser films, due to that the samples I20 and I50 have lower refractive index, compared with those with the same flow rates in series T. It means that the role of high-energy hydrogen ions in breaking Si─Si bond is also outstanding. For the case of 10 sccm H_2, feeding to 12 cm ion source results in relatively higher refractive index, which may be because argon ions of 8 sccm from 12 cm ion source can assist deposition and reduce the etching impact of hydrogen ions of similarly low flow rate.

Since n of all samples at both 1064 nm and 1550 nm wavelengths shows synchronous changes with the increase of annealing temperature, we present the changes in n at 1064 nm here to highlight the influences of different heat treatment temperatures on n of a-Si and hydrogenated a-Si samples, as shown in Fig. 5. For a-Si coatings, n keeps

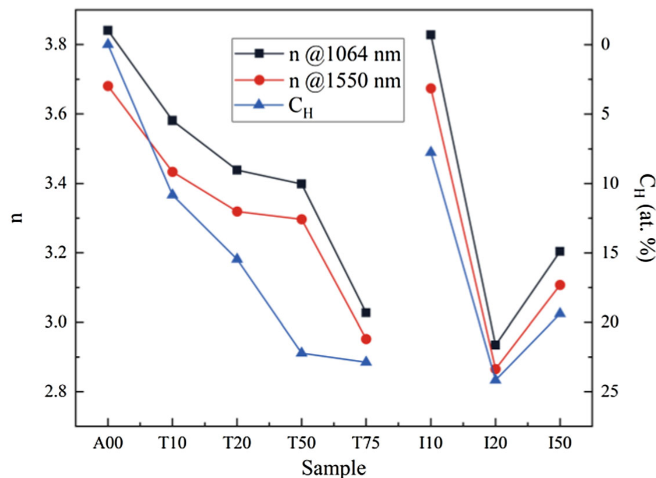

FIG. 4. Refractive index n and hydrogen content C_H for as-deposited samples.

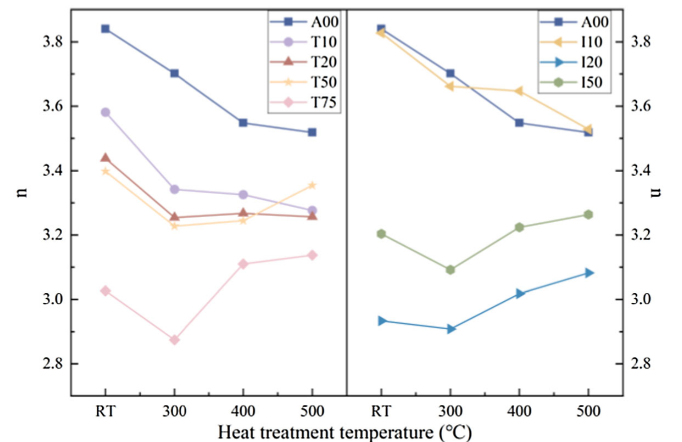

FIG. 5. Refractive index n at 1064 nm as a function of heat treatment temperatures for a-Si and hydrogenated a-Si samples.

decreasing with treatment temperatures increasing. For hydrogenated a-Si, it is found that, in series T, n decreases with the increase of annealing temperature until the flow rate is 20 sccm. When the flow rate is greater than 20 sccm, n decreases first, and then increases with the increase of annealing temperature. A similar phenomenon exists in series I, except that the cutoff of flow rate is 10 sccm. Annealing relaxes the network structure of a-Si coatings and increases the thickness, thus reducing the refractive index and mass density. In regards to hydrogenated a-Si coatings, the effects on refractive index caused by annealing need to be explained from two aspects: network relaxation of silicon and behavior of hydrogen evolution. The former refers to the process of relaxation and reconstruction resulting in low refractive index and mass density, as presented by a-Si coatings. The latter means that, due to postdeposition heat treatment, Si─H bonds break and Si─Si bonds are rebound, which reduces the amounts of "hydrogen substitution" and nanovoids to a certain extent, thus increasing refractive index and mass density. According to the results of the hydrogen content in Table II, the cutoff of flow rate with different trends can also be considered as the cutoff of hydrogen content. When C_H is low, coatings experience some "hydrogen substitution" and nanovoids, and the effect of hydrogen evolution is less obvious than that of silicon network relaxation. This is also applicable to the case where C_H is high but hydrogen diffusion and evolution is small, that is, the heat treatment temperature is low. When C_H is high and heat treatment temperature is high, a large amount of bonded hydrogen is released out of films, and the influence of hydrogen evolution is dominant. Through silicon network relaxation and hydrogen evolution behavior, the variation of n with respect to annealing temperature can be separately understood for each sample, but n of all annealed samples has no obvious overall relationship with the initial C_H or residual C_H. This is not only due to the opposite effects of network relaxation and hydrogen evolution on refractive index and mass density, but also because annealing cannot completely eliminate the initial structural defects [69]. In addition, after annealing, n of the samples in series T is generally higher than that in series I with the same flow rate, except T10 and I10, which is the same as the phenomenon in as-deposited samples. In terms of maintaining the advantage of high refractive index, it is better to introduce hydrogen as molecules.

2. Extinction coefficient

The extinction coefficient k of as-deposited a-Si and hydrogenated a-Si coatings is presented in Fig. 6. The as-deposited a-Si coatings we fabricated have similar k to commercial a-Si coatings [27]. When hydrogen has been introduced, a distinct trend of decreasing k with increasing hydrogen flow rates is found in series T, while k decreases first and then increases with the increase of flow rates in series I. Comparing these trends with the results of C_H, we can find that k decreases with the increase of C_H. According to the relationship between absorption coefficient α and extinction coefficient k ($\alpha = 4\pi k/\lambda$, λ is the wavelength), it can be concluded that the absorption is reducing with the increasing C_H. This law can be explained by the crucial role of hydrogen. Hydrogen can passivate the dangling bonds in a-Si coating, which reduces density of defect states [70–72]. Hydrogen also reduces the density of gap states and moves the valence band down, which increase the optical bandgap [73].

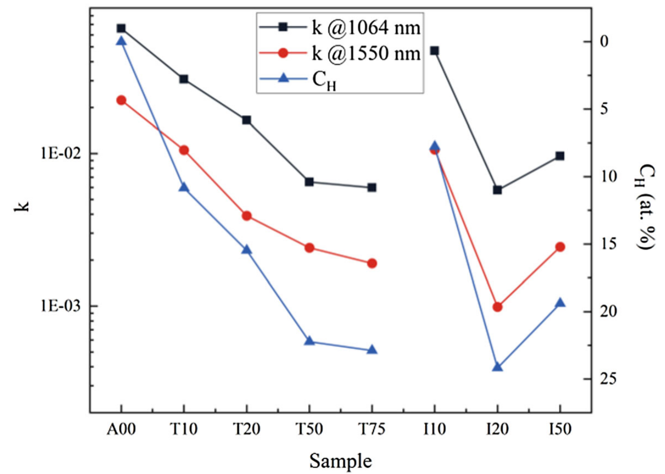

FIG. 6. Extinction coefficient k and hydrogen content $C_H k$ for as-deposited samples.

Figure 7 shows how extinction coefficient k changes with increasing heat treatment temperatures. First of all, k of a-Si coatings decreases with the increase of temperature and reaches the minimum at 500 °C, which is consistent with the work of Ref. [26]. Postdeposition heat treatment has an effect on the structure of silicon network. The absorption can be reduced by atom rearrangement, stress elimination, and defect reduction. Then, effects of heat treatment on k of hydrogenated a-Si coatings also should be considered from two aspects: network relaxation of silicon and behavior of hydrogen evolution. The former has a positive effect on reducing absorption, while the latter has the opposite effect. We can find that k of all hydrogenated a-Si coatings reduces when the temperature is 300 °C, except I20. Considering the data in Table II, after annealing at 300 °C, the combination of the role of hydrogen and the positive impact of heat treatment on the silicon structure would lead to a decrease in k for samples with increased C_H. For samples with decreased C_H, the amount of hydrogen evolution is not significant, thus the positive impact of heat treatment on Si network is more pronounced and k still decreases. After that, with the increase of annealing temperature, k of T10, T20, and I10 keep decreasing while there are almost increases for T50, T75, and I50. This may be because the negative effect of large hydrogen evolution of coatings with higher C_H

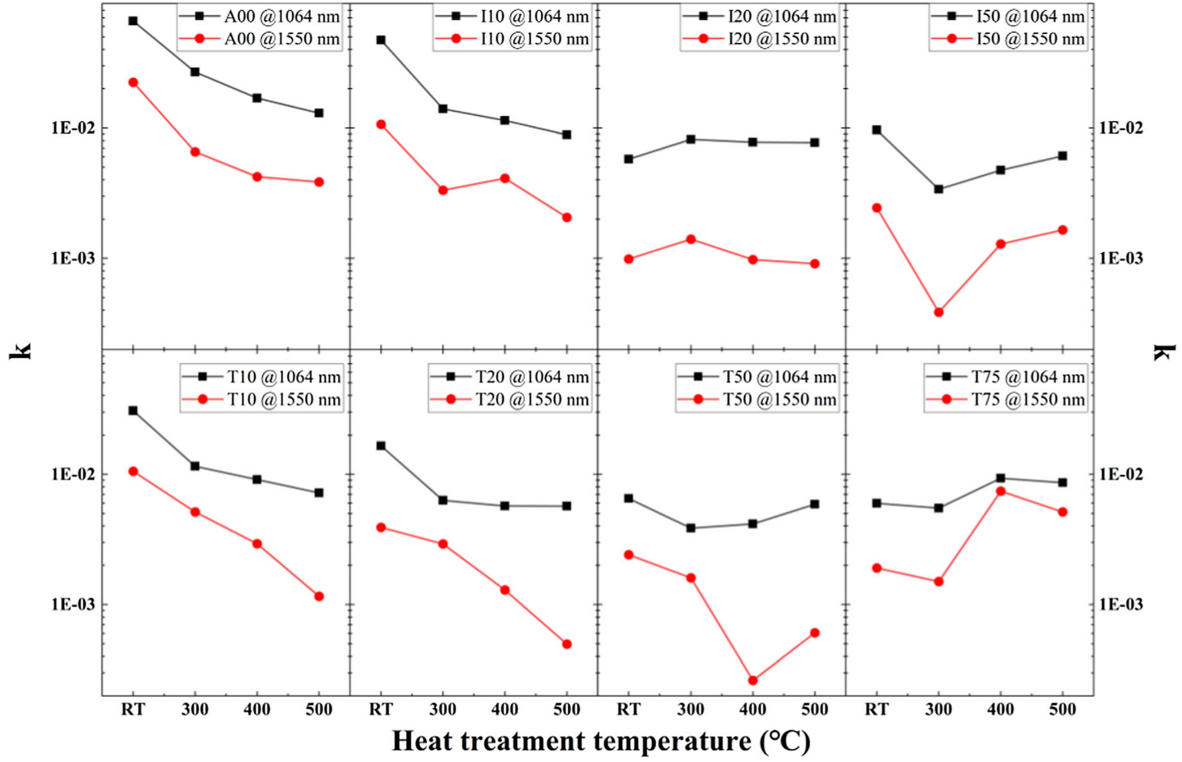

FIG. 7. Extinction coefficient k as a function of heat treatment temperatures for a-Si and hydrogenated a-Si samples.

after annealing has exceeded the positive effect of annealing on Si network. For the sample I20, the trend of k is difficult to explain, which may be related to the possible existence of the most nanovoids caused by energetic hydrogen ions and the highest hydrogen content. Finally, compared with series T and I, the introduction of hydrogen as molecules at the same hydrogen flow rate basically has lower k.

Comprehensively comparing the optical properties of all as-deposited and annealed samples, it can be concluded that sample T50 has the advantages of high refractive index and low k without heat treatment, and its absorption can be further improved after annealing at 300 °C or 400 °C for 1 hour. Compared with of as-deposited a-Si, a reduction by 1 order of magnitude can be achieved via introducing a hydrogen flow rate of 50 sccm to the surface of silicon target. And though the combination of this hydrogenation process with heat treatment at 400 °C for 1 hour, we are able to achieve k of 4.16×10^{-03} at 1064 nm and 2.62×10^{-04} at 1550 nm, approximately lower by about a factor of 16 at 1064 nm and 85 at 1550 nm than k of as-deposited a-Si.

C. Surface morphologies

IBS deposition technology is highly reliable in replicating substrate morphology, which means the intrinsic film roughness can be negligible. This is evident in all of the a-Si and hydrogenated a-Si coatings deposited on superpolished substrates, which all exhibit extremely low RMS roughness. Figure 8 illustrates the typical surface morphologies of as-deposited and annealed a-Si and hydrogenated a-Si coatings. RMS of as-deposited samples A00, I10, and T50 is 0.109 nm, 0.104 nm, and 0.111 nm, respectively. Interestingly, it is found that hydrogen incorporation does not appear to impact the advantage of IBS in terms of intrinsic thin film roughness, despite significant changes to the refractive index. The low scattering loss caused by such low roughness can be expected, which helps to improve the sensitivity and resolution of GW detectors.

Sample T50 provides an example of the moderate effects that postdeposition heat treatment can have on the surface roughness of hydrogenated a-Si coatings. Surface morphologies of companion samples of T50 annealed at 300 °C, 400 °C, and 500 °C are depicted in Figs. 8(d–f), respectively. Corresponding RMS values for these samples are measured to be 0.113 nm, 0.132 nm, and 0.159 nm, respectively. With the increase of annealing temperature, the surface roughness shows a slight increase trend.

Although the surface roughness does not change significantly, some cracks appear on sample T50 after annealing at 500 °C, whereas such cracks does not appear on a-Si coatings. These cracks can be observed via optical microscope, as shown in Fig. 9.

D. Mechanical loss

For the measurements presented in this paper, we excited four resonant modes of each sample at room temperature,

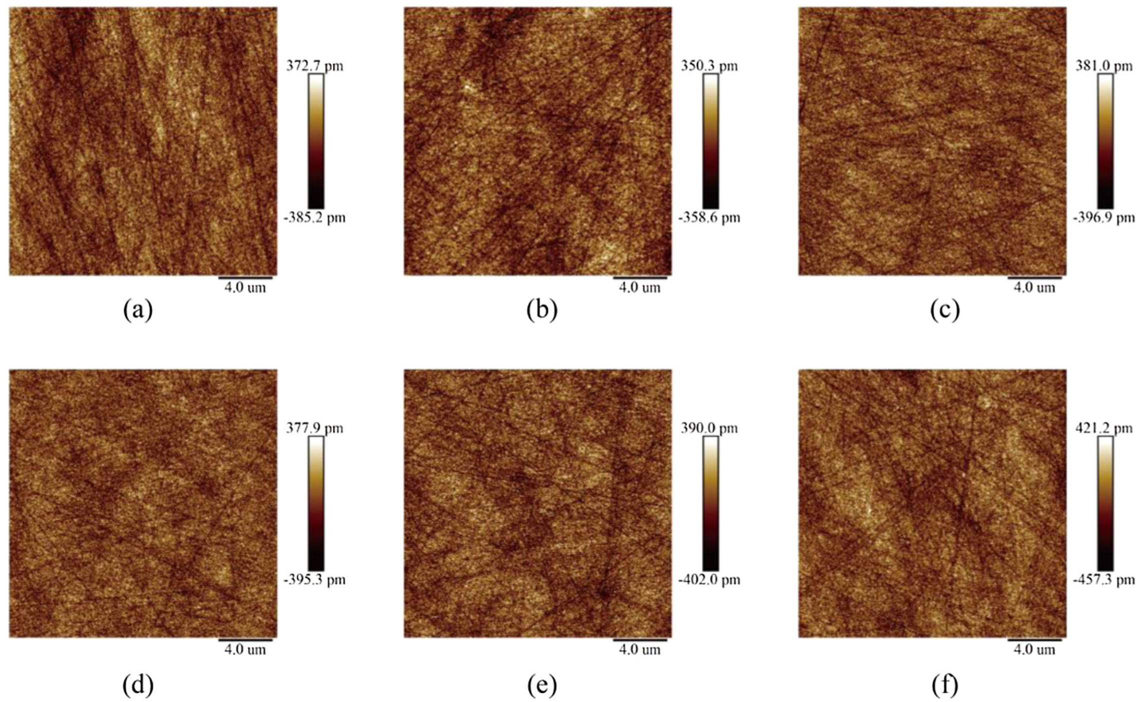

FIG. 8. Typical surface morphologies of a-Si and hydrogenated a-Si coatings. (a) Sample A00 as-deposited, (b) Sample I10 as-deposited, (c) Sample T50 as-deposited, (d) Sample T50 annealed @ 300 °C, (e) Sample T50 annealed @ 400 °C, and (f) Sample T50 annealed @ 500 °C.

which were approximately 1136 Hz, 2604 Hz, 4550 Hz, and 6920 Hz. These resonant modes belong to the same family, namely pure butterfly modes. The test results for mechanical loss of as-deposited a-Si and hydrogenated a-Si coatings at four resonance frequencies are shown in Fig. 10. Since these frequencies are close to each other, we average the mechanical loss values across these frequencies and depict the average values as dashed lines in Fig. 10, in order to better compare the effects of the deposition processes on mechanical loss. As-deposited a-Si coatings in our work have an average mechanical loss of 2.43×10^{-04}, which is consistent with the previously reported mechanical loss of a-Si prepared by IBS technology, ranging from 2.2×10^{-04} to 4.5×10^{-04} [22,27]. It is evident that hydrogen incorporation can reduce the mechanical loss of a-Si, with a maximum reduction by 51% achieved via introducing 10 sccm H_2 to the target. The mechanical loss of other hydrogenated a-Si samples is comparable. However, the underlying reasons for this phenomenon are not yet fully understood and could be attributed to the competition of three mechanisms: passivation of dangling bonds, improvement of silicon atomic network structure, and variation of mass density. Hydrogenation can effectively passivate dangling bonds and alleviate the stress of the network structure, thereby reducing the coating mechanical loss. However, the incorporation of hydrogen could also lead to a decrease in mass density and the formation of nanovoids, which is not conducive to improving mechanical loss. Due to the delicate balance of these mechanisms, there is no clear relationship or rule governing the relationship between C_H and mechanical loss. We speculate that the variation in mechanical loss appears to be more closely related to the changes in silicon atomic network structure induced by hydrogenation, as hydrogenated a-Si exhibits similar levels of mechanical loss, despite having significantly different C_H. Certainly, the achievement of reducing

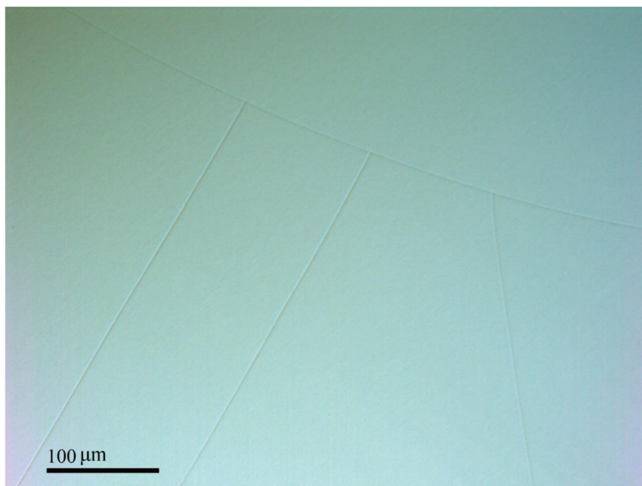

FIG. 9. Surface cracks on sample T50 after 500 °C heat treatment.

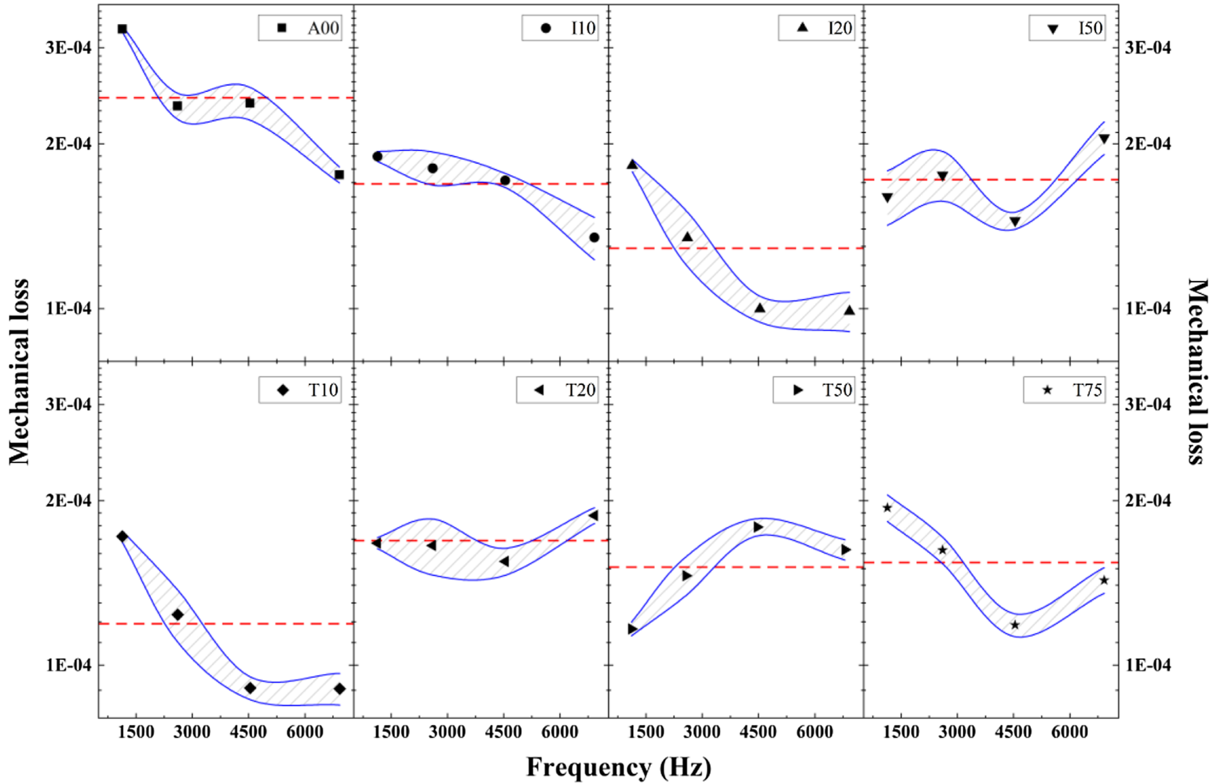

FIG. 10. Coating mechanical loss of as-deposited samples as a function of frequencies. The red dashed line indicates the average mechanical loss value for the corresponding sample. Shaded regions represent error bands.

mechanical loss through the incorporation of hydrogen in IBS deposition is remarkable and deserving of acknowledgement.

Annealing proves to be a highly effective method to improve the mechanical loss of the coatings. We used A00 and T50 as representative examples of a-Si and hydrogenated a-Si coatings, respectively, to demonstrate the effect of different heat treatment temperatures on mechanical loss, as shown in Fig. 11. The reason we selected sample T50 is that it exhibits the best optical properties, while hydrogenated a-Si coatings almost have similar mechanical loss. We observe that for A00 and T50, the mechanical loss initially decrease and then increase with increasing annealing temperature, with the lowest mechanical loss observed after heat treatment at 400 °C. Following annealing, the mechanical loss of a-Si is reduced by up to 85% at its minimum, while the hydrogenated a-Si was reduced by 87% at its minimum. C_H in the hydrogenated a-Si has varied greatly with heat treatment, but the proportion of decrease in mechanical loss is similar to that of a-Si. This may also indicate that the silicon atomic network structure, rather than the hydrogen element, has a greater impact on mechanical loss. Through the combined process of hydrogenation and postdeposition heat treatment, the mechanical loss of a-Si can be further reduced by up to 12-fold. The average mechanical loss of sample T50 annealed at 400 °C was measured to be 2.03×10^{-5}, which is 1 order of magnitude lower than that of $TiO_2:Ta_2O_5$ [74]. The variations in mechanical loss of a-Si and hydrogenated a-Si due to heat treatment appear to be primarily linked to the relaxation of the silicon network structure, as evidenced by similar trends in the mechanical loss changes observed in both materials with increasing annealing temperature. Additionally, despite substantial hydrogen evolution, hydrogenated a-Si still exhibits a decrease in mechanical loss. This further reinforces the connection between silicon network structure relaxation and mechanical loss variations in these materials. It is worth noting that the mechanical loss of T50 annealed at 500 °C should have been lower, but due to the presence of surface cracks (as shown in Fig. 9), there was additional loss incurred.

E. Atomic structures

By analyzing the electron diffraction pattern with the eRDF Analyser software [75], we obtained the atomic structure information of the amorphous coating and described it using RDF as shown in Fig. 12. Since electron diffraction is not sensitive to hydrogen element, the RDFs in this paper reflects the atomic structural information of the silicon network. That is acceptable, as the analysis outlined in Sec. IV. D suggests that mechanical loss variations are most likely linked to the atomic structure

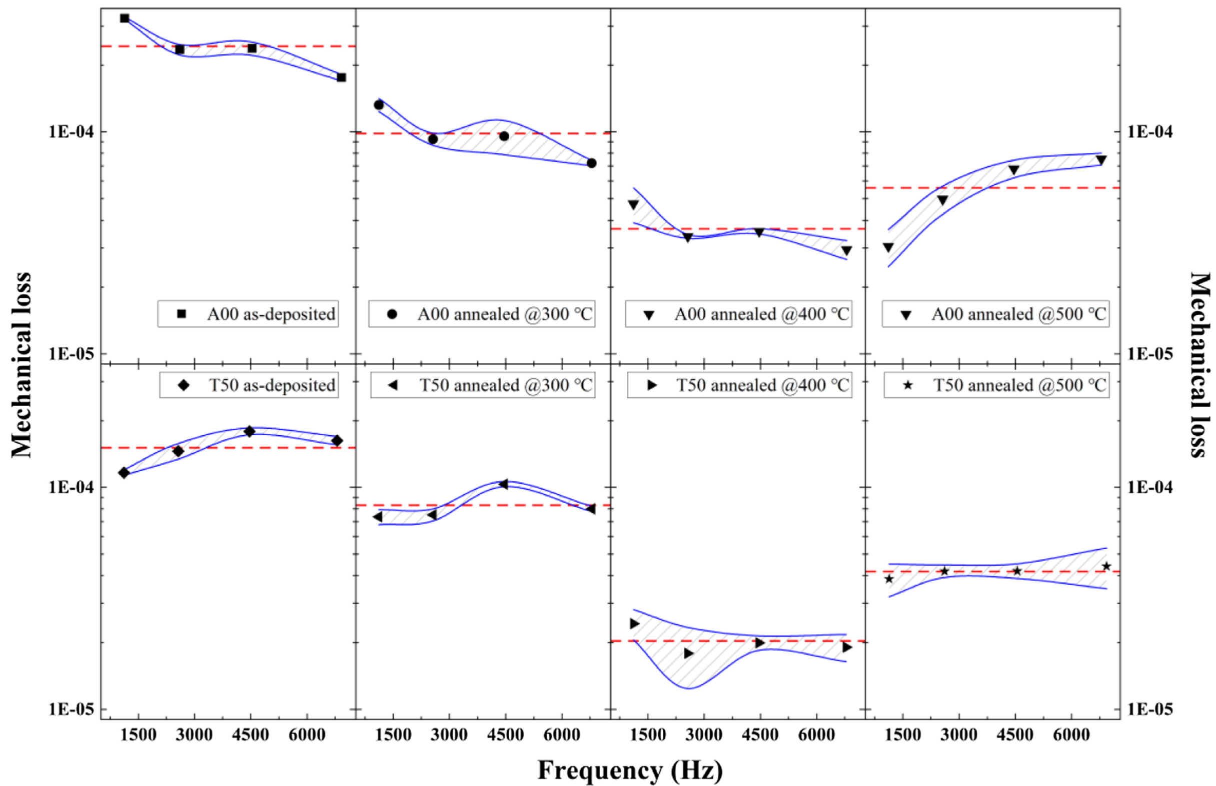

FIG. 11. Coating mechanical loss of as-deposited and annealed samples A00 and T50 as a function of frequencies. The red dashed line indicates the average mechanical loss value for the corresponding sample. Shaded regions represent error bands.

of the silicon network. Similarly, using samples A00 and T50 as representatives of a-Si and hydrogenated a-Si coatings, it can be seen that both a-Si and hydrogenated a-Si have four peaks within 10 Å, which are labeled as P1, P2, P3, and P4. For the as-deposited a-Si, the RDF shows

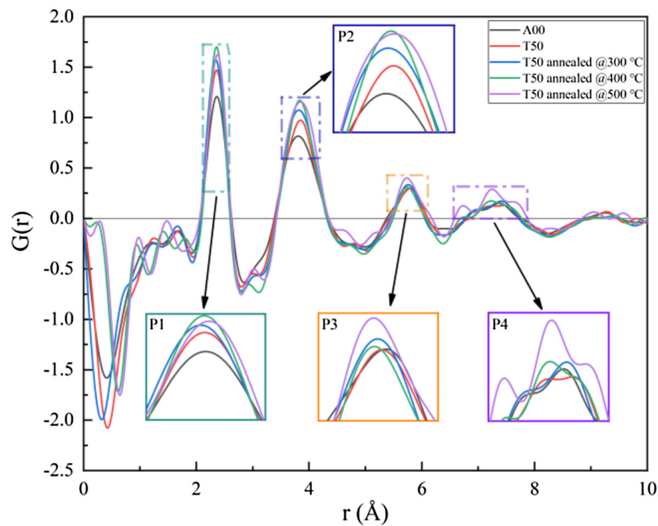

FIG. 12. RDFs of as-deposited sample A00 and as-deposited and annealed samples T50. The four peaks are magnified in the insert to highlight the changes caused by hydrogenation and annealing and are labeled as P1, P2, P3, and P4.

one peak at 2.36 Å, 3.81 Å, and 5.81 Å, and a bifurcated peak at 7.38 Å. For the as-deposited hydrogenated a-Si, the RDF shows one peak at 2.36 Å, 3.85 Å, and 5.78 Å, and a bifurcated peak at 7.48 Å. The peak positions of a-Si and hydrogenated a-Si are consistent with other researches, and the RDFs are also similar [76,77]. The positions of peaks also indicate that P1 and P2 offer insights into the SRO of the silicon network, while peaks P3 and P4 reflect the MRO. After annealing, each peak position of hydrogenated a-Si shows slight variation, while its intensity and full width at half-maximum (FWHM) also change significantly. Additionally, peak P4 changes from a bifurcated peak to a trifurcated peak gradually. The main variations of the four peaks in the RDF are magnified and shown in the insert of Fig. 12. In order to highlight the relevant atomic structural changes that contribute to variations in mechanical loss, we compare the intensity and FWHM of specific peaks, as well as the average mechanical loss. However, we must note that the mechanical loss value of sample T50 annealed at 500 ℃ is not sufficiently accurate due to the presence of cracks. Additionally, peak P4 is a furcated peak, and therefore, we only compared the intensity and FWHM of three peaks P1, P2, and P3 across four samples A00, T50, T50 annealed at 300 ℃, and T50 annealed at 400 ℃.

Figure 13 depicts a comparison of peak intensity and average mechanical loss. It is evident that for as-deposited a-Si and hydrogenated a-Si, the presence of hydrogen

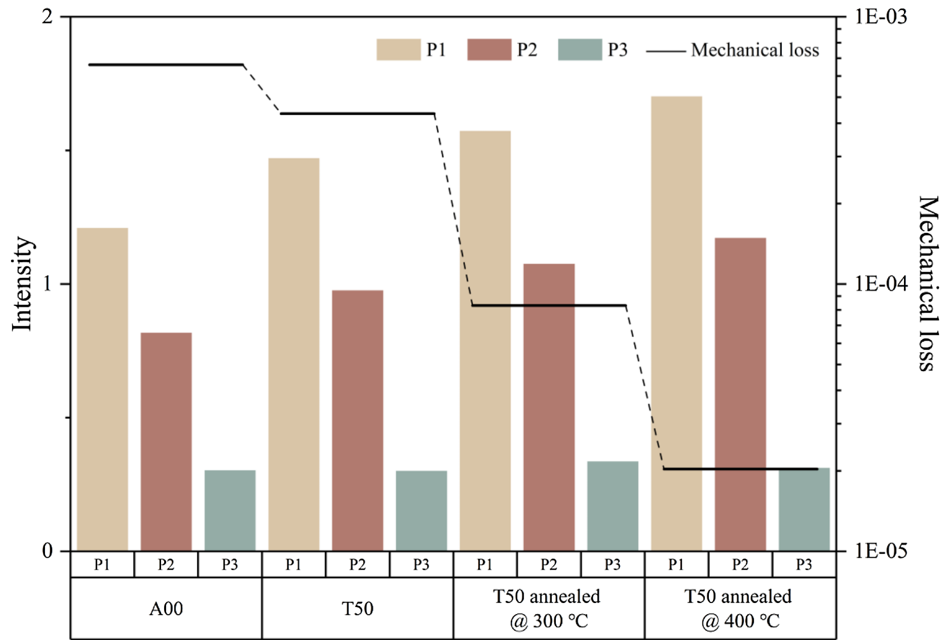

FIG. 13. Peak intensity and average mechanical loss for a-Si and hydrogenated a-Si coatings. The bar chart shows the peak intensity, and the black line indicates average coating mechanical loss.

causes an increase in the intensity of peaks P1 and P2, while the intensity of P3 remains mostly unaffected, accompanied by a decrease in average mechanical loss. Similarly, after annealing hydrogenated a-Si at different temperatures, comparable trends are observed, with an increase in the intensity of P1 and P2 and a decrease in average mechanical loss. As the increase in intensity implies an increase in order, it suggests that both hydrogenation and annealing can enhance the optimization of the silicon atomic structure in the short range. Upon comparing data from the four samples, it becomes obvious that the decrease in average mechanical loss can be correlated with an increase in SRO.

In Fig. 14, a comparison of FWHM of peaks and average mechanical loss is presented. It can be observed from as-deposited coatings that the FWHM of all three peaks,

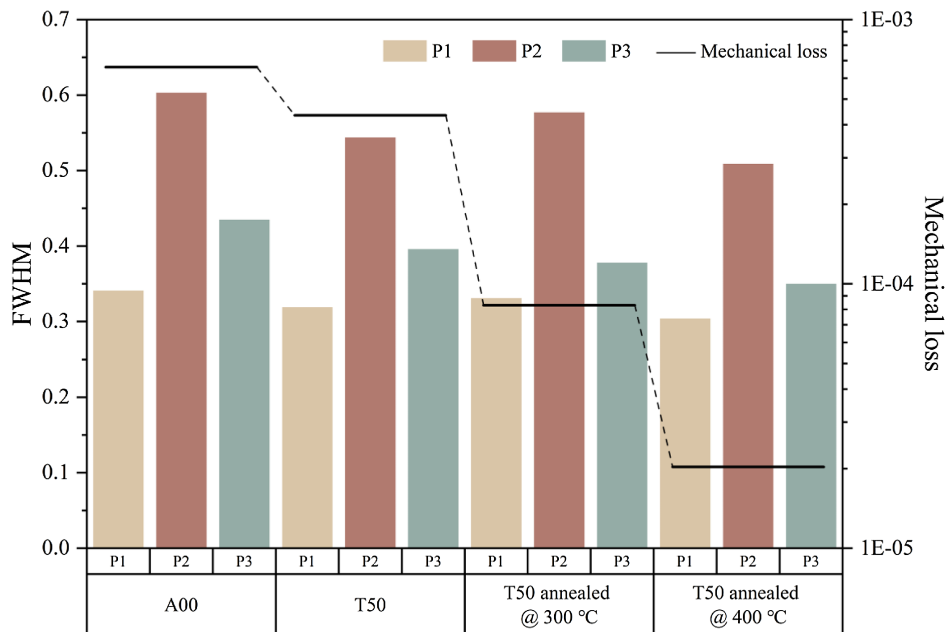

FIG. 14. FWHM of peaks and average mechanical loss for a-Si and hydrogenated a-Si coatings. The bar chart shows the peak intensity, and the black line indicates average coating mechanical loss.

P1, P2, and P3, decreases after hydrogen incorporation, resulting in a decrease in the average mechanical loss. As the decrease in FWHM also suggests an enhancement in order, the hydrogenation process positively influences both the short and medium range structures. In terms of annealed hydrogenated a-Si, the decrease in average mechanical loss is accompanied by a reduction in the FWHM of P3, indicating that annealing enhances the structure in the medium range. Furthermore, based on a comprehensive analysis of data obtained from the four samples, it appears that the decrease in average mechanical loss is invariably accompanied by a decrease in the FWHM of P3, which suggests that enhancing the structure in the medium range of the material and increasing the MRO is effective in reducing coating mechanical loss. In addition, there is a general trend indicating an increase in the SRO with the average mechanical loss decreasing, even though there is a deviation in the FWHM of P1 and P2 observed in sample T50 annealed at 300 °C, which does not decrease.

V. CONCLUSION

We have decreased the optical absorption and mechanical loss of IBS a-Si coatings by introducing hydrogen during coating deposition. With IBS technology, all a-Si and hydrogenated a-Si coatings have good surface quality. We have investigated the influences of different ways to introduce hydrogen into silicon network and postdeposition heat treatment temperature on the properties of a-Si and hydrogenated a-Si coatings.

Different hydrogen introduction processes can lead to different C_H, but a higher hydrogen flow rate generally results in an increased C_H in the coatings. When hydrogen is introduced as a molecule, C_H steadily increases with the increase of hydrogen flow rate. When hydrogen is introduced as a high-energy ion, its role in breaking Si─H and Si─Si bonds causes a drastic change in C_H. Annealing also leads to significant changes in C_H, which is difficult to explain due to the delicate balance of diffusion, relocation, and evolution of hydrogen. However, it can be observed that the initial C_H and heat treatment temperature are important influencing factors.

The trend of refractive index decreasing with increasing C_H is obvious. This can be explained by “hydrogen substitution”, and nanovoids contained in hydrogenated a-Si coatings may increase with higher C_H. A large amount of high-energy hydrogen ions can also reduce the refractive index by breaking Si─Si bond and forming more nanovoids. The effects of annealing on the refractive index depend on two aspects: network relaxation of silicon and behavior of hydrogen evolution, with the former reducing the refractive index and the latter increasing it. When C_H changes little, the relaxation of the silicon network dominates, and the refractive index decreases. When the amount of hydrogen evolution is significant, the influence of hydrogen evolution dominates, and the refractive index increases.

Hydrogenation significantly reduces optical absorption of a-Si by passivating the dangling bonds of a-Si, and the extinction coefficient decreases with the increase of C_H. The influences of heat treatment on extinction coefficient also can be considered from two aspects: network relaxation of silicon and behavior of hydrogen evolution, with the former reducing absorption and the latter increasing absorption. When C_H changes little, the relaxation of the silicon network becomes the dominant factor, leading to a decrease in the extinction coefficient. However, when a significant amount of hydrogen evolution occurs, the influence of hydrogen evolution becomes the primary factor, resulting in an increase in the extinction coefficient. The beneficial effects of silicon atom rearrangement and network relaxation on absorption improvement can outweigh the negative effects of hydrogen evolution, provided that the annealing temperature is appropriate.

Since high-energy hydrogen ions possess the ability to break Si─Si and Si─H bonds, it is better to introduce hydrogen as a molecule on improving the optical properties of a-Si by feeding hydrogen gas to surface of the silicon target. The total concentration of hydrogen is a key factor in determining the changes in optical properties of as-deposited coatings. Hydrogenated a-Si coatings prepared by introducing a hydrogen flow rate of 50 sccm to the surface of silicon target exhibit the best optical properties, with the extinction coefficient lower by 1 order of magnitude than that of a-Si coatings. And subjecting the coatings to proper heat treatment can further reduce absorption. Through hydrogenation and heat treatment at 400 °C for 1 hour, the extinction coefficient of a-Si can be reduced by about a factor of 16 at 1064 nm and 85 at 1550 nm.

Hydrogenation improves the coating mechanical loss of a-Si, and the highest reduction in mechanical loss can reach up to 51% with appropriate hydrogenation processes. Annealing can also reduce mechanical loss of a-Si, with a maximum reduction of 85% by annealing at 400 °C for 1 hour. Combining appropriate postdeposition heat treatment with the best hydrogenation process for optical properties, coating mechanical loss of a-Si can be reduced by a factor of 12, which is 1 order of magnitude lower than that of $TiO_2:Ta_2O_5$. The effects of hydrogenation or annealing on the coating mechanical loss seem to be more closely related to changes in the silicon network structure. We can gain insights into the mechanism underlying the decrease in coating mechanical loss at the atomic scale by examining changes in the atomic structure of the silicon network. It can be seen that hydrogenation and annealing increase the short-range order and medium-range order of the silicon network, resulting in a decrease in mechanical loss.

Hydrogenation and annealing are effective methods for enhancing the optical and mechanical properties of IBS a-Si coatings. Combining these two processes is expected to be utilized in future a-Si coating preparation, leading to further improvements in the potential application of a-Si in gravitational wave detection with IBS technology.

ACKNOWLEDGMENTS

This work was supported by National Natural Science Foundation of China (NSFC) (Grants No. 61975155, No. 62061136008, No. 61925504, No. 62192770, and No. 62192772), and Fundamental Research Funds for the Central Universities.

[1] R. X. Adhikari, Rev. Mod. Phys. **86**, 121 (2014).
[2] Y. Y. Jiang, A. D. Ludlow, N. D. Lemke, R. W. Fox, J. A. Sherman, L. S. Ma, and C. W. Oates, Nat. Photonics **5**, 158 (2011).
[3] V. K. Sakharov, Tech. Phys. **56**, 1135 (2011).
[4] A. Matsugi and A. Miyoshi, Chem. Phys. Lett. **521**, 26 (2012).
[5] B. P. Abbott *et al.* (LIGO Scientific Collaboration and Virgo Collaboration), Phys. Rev. Lett. **116**, 061102 (2016).
[6] B. P. Abbott *et al.* (LIGO Scientific Collaboration and Virgo Collaboration), Phys. Rev. Lett. **116**, 131103 (2016).
[7] G. M. Harry *et al.*, Classical Quantum Gravity **19**, 897 (2002).
[8] H. B. Callen and R. F. Greene, Phys. Rev. **86**, 702 (1952).
[9] M. Granata *et al.*, Classical Quantum Gravity **37**, 095004 (2020).
[10] S. D. Penn *et al.*, Classical Quantum Gravity **20**, 2917 (2003).
[11] D. R. M. Crooks *et al.*, Classical Quantum Gravity **21**, S1059 (2004).
[12] J. Aasi *et al.* (LIGO Scientific Collaboration), Classical Quantum Gravity **32**, 074001 (2015).
[13] F. Acernese *et al.*, Classical Quantum Gravity **32**, 024001 (2015).
[14] I. Martin *et al.*, Classical Quantum Gravity **25**, 055005 (2008).
[15] I. W. Martin *et al.*, Classical Quantum Gravity **27**, 225020 (2010).
[16] K. Somiya for the KAGRA Collaboration, Classical Quantum Gravity **29**, 124007 (2012).
[17] Y. Sakakibara *et al.*, Classical Quantum Gravity **31**, 224003 (2014).
[18] M. Punturo *et al.*, Classical Quantum Gravity **27**, 084007 (2010).
[19] M. Punturo *et al.*, Classical Quantum Gravity **27**, 194002 (2010).
[20] S. Hild *et al.*, Classical Quantum Gravity **28**, 094013 (2011).
[21] S. Hild, Classical Quantum Gravity **29**, 124006 (2012).
[22] P. G. Murray, I. W. Martin, K. Craig, J. Hough, R. Robie, S. Rowan, M. R. Abernathy, T. Pershing, and S. Penn, Phys. Rev. D **92**, 062001 (2015).
[23] X. Liu, D. R. Queen, T. H. Metcalf, J. E. Karel, and F. Hellman, Phys. Rev. Lett. **113**, 025503 (2014).
[24] K. U. M. Kumar and M. G. Krishna, Semicond. Sci. Technol. **23**, 105020 (2008).
[25] J. Steinlechner, I. W. Martin, R. Bassiri, A. Bell, M. M. Fejer, J. Hough, A. Markosyan, R. K. Route, S. Rowan, and Z. Tornasi, Phys. Rev. D **93**, 062005 (2016).
[26] J. Steinlechner, I. W. Martin, A. S. Bell, J. Hough, M. Fletcher, P. G. Murray, R. Robie, S. Rowan, and R. Schnabel, Phys. Rev. Lett. **120**, 263602 (2018).
[27] R. Birney *et al.*, Phys. Rev. Lett. **121**, 191101 (2018).
[28] J. Steinlechner, A. Khalaidovski, and R. Schnabel, Classical Quantum Gravity **31**, 105005 (2014).
[29] W. B. Jackson and N. M. Amer, Phys. Rev. B **25**, 5559 (1982).
[30] S. Scaglione, C. Coluzza, D. Dellasala, L. Mariucci, A. Frova, and G. Fortunato, Thin Solid Films **120**, 215 (1984).
[31] H. Windischmann, R. W. Collins, and J. M. Cavese, J. Non-Cryst. Solids **85**, 261 (1986).
[32] P. J. Martin, R. P. Netterfield, W. G. Sainty, and D. R. Mckenzie, Thin Solid Films **100**, 141 (1983).
[33] J. Steinlechner, I. W. Martin, J. Hough, C. Kruger, S. Rowan, and R. Schnabel, Phys. Rev. D **91**, 042001 (2015).
[34] W. Yam, S. Gras, and M. Evans, Phys. Rev. D **91**, 042002 (2015).
[35] S. C. Tait *et al.*, Phys. Rev. Lett. **125**, 011102 (2020).
[36] J. Degallaix *et al.*, J. Opt. Soc. Am. A **36**, C85 (2019).
[37] L. Pinard *et al.*, Appl. Opt. **56**, C11 (2017).
[38] X. Liu, B. E. White, R. O. Pohl, E. Iwanizcko, K. M. Jones, A. H. Mahan, B. N. Nelson, R. S. Crandall, and S. Veprek, Phys. Rev. Lett. **78**, 4418 (1997).
[39] X. Liu and R. O. Pohl, Phys. Rev. B **58**, 9067 (1998).
[40] X. Liu, C. L. Spiel, R. D. Merithew, R. O. Pohl, B. P. Nelson, Q. Wang, and R. S. Crandall, Mater. Sci. Eng. A **442**, 307 (2006).
[41] B. P. Abbott *et al.* (LIGO Scientific Collaboration and Virgo Collaboration), Classical Quantum Gravity **34**, 044001 (2017).
[42] M. Morita, T. Ohmi, E. Hasegawa, M. Kawakami, and M. Ohwada, J. Appl. Phys. **68**, 1272 (1990).
[43] OptiLayer Thin Film Software, https://www.optilayer.org (Accessed December 2022).
[44] W. H. Wang and S. Chao, Opt. Lett. **23**, 1417 (1998).
[45] E. Cesarini, M. Lorenzini, E. Campagna, F. Martelli, F. Piergiovanni, F. Vetrano, G. Losurdo, and G. Cagnoli, Rev. Sci. Instrum. **80**, 053904 (2009).
[46] G. Vajente *et al.*, Classical Quantum Gravity **35**, 075001 (2018).
[47] T. J. Li *et al.*, Phys. Rev. D **89**, 092004 (2014).
[48] COMSOL Multiphysics, https://www.comsol.com (Accessed December 2022).

[49] Y. Qin, H. Yan, F. Li, L. Qiao, Q. Liu, and D. He, Appl. Surf. Sci. **257**, 817 (2010).
[50] A. Remolina, B. M. Monroy, M. F. Garcia-Sanchez, A. Ponce, M. Bizarro, J. C. Alonso, A. Ortiz, and G. Santana, Nanotechnology **20**, 245604 (2009).
[51] J. C. Knights, G. Lucovsky, and R. J. Nemanich, J. Non-Cryst. Solids **32**, 393 (1979).
[52] G. Lucovsky, R. J. Nemanich, and J. C. Knights, Phys. Rev. B **19**, 2064 (1979).
[53] J. D. Ouwens and R. E. I. Schropp, Phys. Rev. B **54**, 17759 (1996).
[54] R. Amrani, D. Benlekehal, R. Baghdad, D. Senouci, A. Zeinert, K. Zellama, L. Chahed, J. D. Sib, and Y. Bouizem, J. Non-Cryst. Solids **354**, 2291 (2008).
[55] E. C. Freeman and W. Paul, Phys. Rev. B **18**, 4288 (1978).
[56] N. Maley, Phys. Rev. B **46**, 2078 (1992).
[57] A. A. Langford, M. L. Fleet, B. P. Nelson, W. A. Lanford, and N. Maley, Phys. Rev. B **45**, 13367 (1992).
[58] T. Oh and C. K. Choi, J. Korean Phys. Soc. **56**, 1150 (2010).
[59] J. A. Reimer, R. W. Vaughan, and J. C. Knights, Solid State Commun. **37**, 161 (1981).
[60] J. Baugh, D. Han, Q. Wang, and Y. Wu, Mater. Res. Soc. Symp. Proc. **557**, 383 (1999).
[61] W. Beyer and H. Wagner, J. Non-Cryst. Solids **59–60**, 161 (1983).
[62] H. M. Branz, Solid State Commun. **105**, 387 (1998).
[63] W. Beyer, Phys. Status Solidi A **159**, 53 (1997).
[64] Z. Remes, M. Vanecek, A. H. Mahan, and R. S. Crandall, Phys. Rev. B **56**, R12710 (1997).
[65] E. C. Freeman and W. Paul, Phys. Rev. B **20**, 716 (1979).
[66] A. Matsuda, Thin Solid Films **337**, 1 (1999).
[67] A. Matsuda, J. Non-Cryst. Solids **338–340**, 1 (2004).
[68] R. Biswas and Y.-P. Li, Phys. Rev. Lett. **82**, 2512 (1999).
[69] M. Molina-Ruiz, H. C. Jacks, D. R. Queen, Q. Wang, R. S. Crandall, and F. Hellman, Mater. Res. Express **7**, 095201 (2020).
[70] R. C. Chittick, J. H. Alexander, and H. F. Sterling, J. Electrochem. Soc. **116**, 77 (1969).
[71] P. G. Le Comber and W. E. Spear, Phys. Rev. Lett. **25**, 509 (1970).
[72] M. H. Brodsky, M. Cardona, and J. J. Cuomo, Phys. Rev. B **16**, 3556 (1977).
[73] F. Demichelis, E. Minetti-Mezzetti, A. Tagliaferro, E. Tresso, P. Rava, and N. M. Ravindra, J. Appl. Phys. **59**, 611 (1986).
[74] R. Flaminio, J. Franc, C. Michel, N. Morgado, L. Pinard, and B. Sassolas, Classical Quantum Gravity **27**, 084030 (2010).
[75] J. Shanmugam, K. B. Borisenko, Y.-J. Chou, and A. I. Kirkland, SoftwareX **6**, 185 (2017).
[76] Z. Q. Liu, D. R. McKenzie, D. J. H. Cockayne, and D. M. Dwarte, Philos. Mag. B **57**, 753 (1988).
[77] K. Jarolimek, R. A. de Groot, G. A. de Wijs, and M. Zeman, Phys. Rev. B **79**, 155206 (2009).